Analysis of the FEBEX multi-barrier system including thermoplasticity of unsaturated bentonite

Fabrice Dupray[1], Bertrand François[2] and Lyesse Laloui[1,*,†]

[1]*Laboratory of Soil Mechanics, Swiss Federal Institute of Technology, Lausanne (EPFL), Station 18, 1015, Lausanne, Switzerland*
[2]*Building, Architecture & Town Planning Department, Université Libre de Bruxelles, Avenue F.D. Roosevelt, 50-CPI 194/2, 1050 Bruxelles, Belgium*

SUMMARY

Deep geological repository involving a multibarrier system constitutes one of the most promising options for isolating high-level radioactive waste from the human environment. To certify the efficiency of waste isolation, it is essential to understand the behaviour of confining geomaterial under a variety of environmental conditions. To this end, results from a near-to-real experiment, the full-scale engineered barriers *in situ* experiment, are studied by means of a thermo–hydro–mechanical finite element approach, including a consistent thermoplastic constitutive model for unsaturated soils. Laboratory tests are simulated to calibrate model parameters. The results of the numerical simulations are compared with sensor measurements and show the ability of the model to reproduce the main behavioural features of the system. The influence of the hysteretic and temperature-dependent retention of water on the mechanical response is exhibited. Finally, those results are interpreted in the light of thermoplasticity of unsaturated soils, which reveals the highly coupled and non-linear characters of the processes encountered. Copyright © 2011 John Wiley & Sons, Ltd.

1. INTRODUCTION

Over the coming years, definitive solutions will likely be available for the management of large quantities of high-level radioactive waste that mainly stem from the production of nuclear electricity. Deep geological repositories constitute one of the most promising options for isolating such waste from the human environment. Analysis and predictions about the long-term behaviour of such a disposal method should be based on robust science. In this context, the highly coupled thermo–hydro–mechanical (THM) phenomena that occur in engineered and geological barriers must be captured adequately by means of numerical analysis [1]. To validate and calibrate the mathematical models, numerical simulations of *in situ* experiments reproducing comparable studies have to be performed [2, 3]. In such a way, the results of the experiment may be interpreted within the constitutive framework of the chosen models, which in turn may improve the understanding of the phenomena involved.

The full-scale engineered barriers experiment (FEBEX) in crystalline host rock *in situ* test is a near-to-real experiment carried out in the underground laboratory at Grimsel (Switzerland). It uses the Spanish disposal concept for underground nuclear waste storage in granitic formations as its reference. The gallery, excavated in the granitic rock of the Aare Massif in central Switzerland, has a diameter of

---

*Correspondence to: Lyesse Laloui, Laboratory of Soil Mechanics, Swiss Federal Institute of Technology, Lausanne (EPFL), Station 18, 1015 Lausanne, Switzerland.
†E-mail: lyesse.laloui@epfl.ch

2.28 m and a length of 71.4 m. Two heaters (0.95 m in diameter and 4.54 m long, the same dimensions as the canisters of the reference disposal concept) were placed in the axis of the gallery at a 1-m distance from each other. The free space between the heaters and the granite was filled with compacted bentonite blocks for the last 17 m of the gallery. The 17-m-long test zone was sealed by a concrete plug (Figure 1) [4]. During this *in situ* experiment, direct measurements, in terms of temperature, fluid pressure, humidity, total pressure, and deformation of the confining structure, provided worthwhile information for the verification and the validation of mathematical models aimed at predicting the coupled THM processes occurring in such disposal. Several numerical predictions, or validations, have already been reported in the literature by Gens *et al.* [5–7], Alonso *et al.* [8], Sugita *et al.* [9], Rutqvist and Tsang [10], and Nguyen *et al.* [11], among others. Gens *et al.* [12] recently published a comprehensive article on this *in situ* heating test, including observations, numerical analysis, and interpretation. Experimental aspects considering the system of sensors were especially detailed in this article and will not be further reviewed here. The present study brings additional information on various aspects of the problem; in particular, the role of the irreversible straining of the bentonite, related to its thermoplasticity and suction-induced hardening, is highlighted. In the present article, the use of a constitutive model that considers the plastic strains upon thermal and suction loadings in a unique theoretical framework offers a unified constitutive approach for the modelling of the bentonite response. By doing so, the focus is made on the various THM couplings including important plastic mechanisms in the behaviour of bentonite.

Predictions of the THM behaviour of compacted bentonite and host rock have been performed by means of finite element simulations. These numerical analyses provide accurate information on the mechanical effects of temperature and suction evolution in the confining materials. To carry out the numerical analysis, the ACMEG-TS elasto-thermoplastic constitutive model for unsaturated soils [13] has been implemented in the finite element code LAGAMINE [14, 15].

First, the article presents a summary of the mathematical formulation of the constitutive and numerical tools used and the calibration of the material parameters of the FEBEX bentonite. Then, features of the numerical analysis performed are presented and the comparison between the results obtained and *in situ* measurements is discussed. Finally, we interpret the results obtained in terms of irreversible strains, coupling between mechanical, thermal, and water retention responses and diffusion processes.

2. THEORETICAL FORMULATION

2.1. Equilibrium and balance equations

The balance equations are obtained by considering that the material is composed of a solid matrix and voids filled with liquid and gas phases. The liquid phase is assumed to contain two species: liquid water and dissolved air. Similarly, the gas phase is composed of dry air and water vapour. Temperature changes in the medium may modify the liquid–vapour equilibrium. To uniquely describe the state of the material, four primary state variables are required: gas pressure p_g, water pressure p_w, temperature
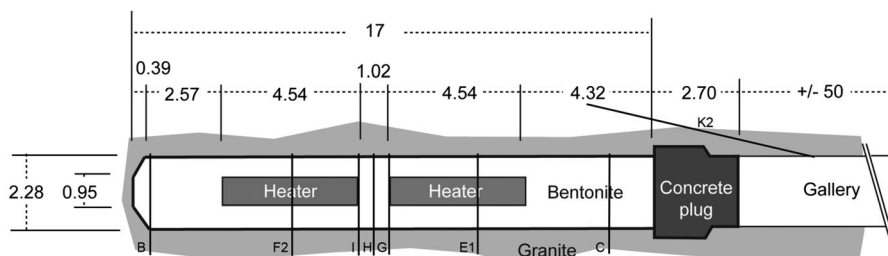

Figure 1. Layout of the FEBEX *in situ* test, with localisation of the sections and boreholes (adapted from Gens *et al.* [12]).

T, and solid displacement vector $\mathbf{u}$. The intrinsic solid-phase component is assumed to be incompressible (incompressible grains), whereas the water phase is slightly compressible. The solid, liquid, and gas phases are assumed to be in thermal equilibrium, and a unique temperature is defined at each node. This assumption is justified by the relatively slow kinematics of the governing processes, which allow a continuous thermal equilibrium between phases.

The compositional approach [16] is used to write the balance equations, which means that the mass balances are described for the components (also called species) present in the mixture rather than for the phases. Therefore, the conservation of mass of each chemical species (water and air) is assumed. Using this approach, the phase exchange term will cancel in the balance equations. In the following equations, the subscripts l, g, w, da, a, and v are related to the liquid phase, the gas phase, the liquid water, the dissolved air in water, the dry air, and the water vapour, respectively. The governing equations presented are taken from Refs. [15, 17, 18], where further details can be found.

The equilibrium and balance equations, as well as the water and heat flows, are expressed in the moving current configuration through a Lagrangian updated formulation [19]. According to these assumptions, the mass balance equation of the solid skeleton is necessarily met. For a given mixture volume, V, the mass balance equation reads

$$\frac{\partial \rho_s (1-n)V}{\partial t} = 0 \tag{1}$$

where ρ_s is the density of solid grains, n is the soil porosity, and t is the time.

The mass conservation equations for the water and gas species are, respectively,

$$\underbrace{\frac{\partial}{\partial t}(\rho_w n S_r) + div(\rho_w \mathbf{f_l}) - Q_w +}_{\text{Liquid water}} \underbrace{\frac{\partial}{\partial t}(\rho_v n(1-S_r)) + div(\mathbf{i_v} + \rho_v \mathbf{f_g}) - Q_v}_{\text{Water vapour}} = 0 \tag{2}$$

$$\underbrace{\frac{\partial}{\partial t}(\rho_a n(1-S_r)) + div(\rho_a \mathbf{f_g} + \mathbf{i_a}) - Q_a}_{\text{Dry air in gas phase}} + \underbrace{\frac{\partial}{\partial t}(\rho_a H_s n S_r) + div(\rho_a H_{aw} \mathbf{f_l}) - Q_{da}}_{\text{Dissolved air in water}} = 0 \tag{3}$$

where ρ_w, ρ_v, and ρ_a are the bulk density of liquid water, water vapour, and dry air, respectively. $\mathbf{f_l}$ and $\mathbf{f_g}$ are the macroscopic velocity of the liquid and gas phases, respectively. $\mathbf{i_v}$ and $\mathbf{i_a}$ are the non-advective flux of water vapour and dry air, respectively. S_r is the degree of saturation. The dimensionless Henry's law constant, H_{aw}, defining the proportion of dissolved air in the liquid phase, is taken to be equal to 0.017 (combined value for nitrogen and oxygen at 25°C, [17]). Q_w, Q_v, Q_a, and Q_{da} are volume sources of liquid water, water vapour, dry air, and dissolved air in water, respectively.

The energy balance equation of the mixture has the following form:

$$\underbrace{\frac{\partial S_T}{\partial t} + L\frac{\partial}{\partial t}(\rho_v n(1-S_r))}_{\text{Heat storage}} + \underbrace{div(\mathbf{f_T}) + L \cdot div(\mathbf{i_v} + \rho_v \mathbf{f_g})}_{\text{Heat transfer}} - Q_T = 0 \tag{4}$$

where $\mathbf{f_T}$ is the heat flow and Q_T is a volume heat source. L is the latent heat of water vaporisation. The enthalpy of the system S_T is given by

$$S_T = \rho C_p (T - T_0) \tag{5}$$

where ρ and C_p are the density and the specific heat of the mixture (solid matrix with voids filled by gas and liquid), respectively. Those parameters are deduced from the properties of each phase:

$$\rho C_p = n S_r \rho_w c_{p,w} + (1 - n)\rho_s c_{p,s} + n(1 - S_r)\rho_a c_{p,a} + n(1 - S_r)\rho_v c_{p,v} \tag{6}$$

where ρ_s is the soil grain bulk density and $c_{p,w}$, $c_{p,s}$, $c_{p,a}$, and $c_{p,v}$ are the specific heat of liquid water, solid, dry air, and water vapour, respectively.

The soil equilibrium equation is given by

$$div(\boldsymbol{\sigma}) + \mathbf{b} = 0 \tag{7}$$

where $\boldsymbol{\sigma}$ is the total (Cauchy) stress tensor, with compressive stress taken as positive, and $\mathbf{b}$ is the body force vector, which is equal to $\rho \mathbf{g}$ if the only body force is gravity.

2.2. Constitutive relations

The conservation equations that govern the THM equilibrium of the system (Equations (1) to (7)) need to be expressed in terms of the primary state variables ($\mathbf{u}$, p_w, p_g and T) after the introduction of the constitutive relationships detailed in the next paragraphs. The liquid water bulk density depends on the pore water pressure p_w and temperature T through the water bulk modulus χ_w and the volumetric water thermal expansion coefficient β'_w:

$$\rho_w = \rho_{w0}\left(1 + \frac{p_w - p_{w0}}{\chi_w} - \beta'_w(T - T_0)\right) \tag{8}$$

where ρ_{w0}, p_{w0}, and T_0 are the initial values of water bulk density, pore water pressure, and temperature, respectively. The bulk density of the water vapour is determined through the following equations:

$$\rho_v = \exp\left(\frac{(p_w - p_g)M_v}{R T \rho_w}\right)\frac{p_{v,0}M_v}{R T} \tag{9}$$

where p_w and p_g are the liquid water and gas pressures, respectively, M_v is the vapour molar mass (=0.018 kg/mol), T is temperature expressed in kelvin, and $p_{v,0}$ is the saturated vapour pressure given by an experimental expression dependent on temperature [17, 20]:

$$p_{v,0} = a \exp(-b/T) \tag{10}$$

with $a = 112\,659$ MPa and $b = 5192.74$ K for a temperature range between 273 and 373 K.

The bulk density of dry air can be deduced considering that the gas phase is an ideal gas to which the Dalton law can be applied:

$$p_g = p_a + p_v \tag{11}$$

Consequently, the bulk density of dry air is

$$\rho_a = \frac{p_a M_a}{R T} = \frac{(p_g - p_v)M_a}{R T} = \frac{p_g M_a}{R T} - \frac{\rho_v M_a}{M_v} \tag{12}$$

where M_a is the dry air molar mass (= 28.8×10^{-3} kg/mol).

The liquid phase motion is governed by the Darcy's law:

$$\mathbf{f_l} = -\frac{\mathbf{k_w}}{\mu_w}\mathbf{grad}(p_w) \tag{13}$$

where $\mathbf{k_w}$ is the tensor of intrinsic water permeability and μ_w is the dynamic viscosity of the water. The water permeability, assumed isotropic ($\mathbf{k_w} = k_w\mathbf{I}$, $\mathbf{I}$ being the identity matrix), depends on the degree of saturation S_r according to the following equation:

$$k_w = k_{w,sat} S_r{}^{CKW1} \tag{14}$$

where CKW1 is a material parameter. $k_{w,sat}$ is the saturated permeability, which depends on the soil porosity n through the Kozeny–Carman relation:

$$k_{w,sat} = k_{w0,sat} \frac{n^{EXPN}}{(1-n)^{EXPM}} \frac{(1-n_0)^{EXPM}}{n_0{}^{EXPN}} \tag{15}$$

where $k_{w0,sat}$ is the saturated water permeability corresponding to the reference porosity n_0 and *EXPN* and *EXPM* are material parameters of the Kozeny–Carman relation.

The dynamic viscosity of water is calculated through the relationship proposed by Thomas and King [21], which is valid for a large range of temperatures:

$$\mu_w = 0.6612(T - 229)^{-1.562} \tag{16}$$

where μ_w is the dynamic viscosity of water in Pa s and T is the temperature in kelvin. In Equation (13), it is assumed that ρ_w, $\mathbf{k_w}$, and μ_w are unaffected by the amount of dissolved air in the liquid phase.

The non-advective flux of water vapour diffusion is related to the air bulk density gradient:

$$\mathbf{i_v} = n(1 - S_r)\tau D\rho_g \mathbf{grad}\left(\frac{\rho_a}{\rho_g}\right) = -\mathbf{i_a} \tag{17}$$

where D is the air diffusion coefficient expressed according to the work of Philip and De Vries [22]:

$$D = 5.893 \ 10^{-6} \frac{T^{2.3}}{p_g} \tag{18}$$

where D, T, and p_g are expressed in m^2/s, kelvin, and Pascal, respectively. τ is the tortuosity of the material.

The heat transport is governed by conduction and convection:

$$\mathbf{f_T} = -\Gamma\mathbf{grad}(T) + \left[c_{p,w}\rho_w\mathbf{f_w} + c_{p,a}\left(\mathbf{i_a} + \rho_a\mathbf{f_g}\right) + c_{p,v}\left(\mathbf{i_v} + \rho_v\mathbf{f_g}\right)\right](T - T_0) \tag{19}$$

where Γ is the thermal conductivity of the mixture as deduced from the thermal conductivity of each phase:

$$\Gamma = \lambda_s(1 - n) + \lambda_w n S_r + \lambda_g n(1 - S_r) \tag{20}$$

where λ_s, λ_w, and λ_a are the thermal conductivity of the solid, liquid, and gas phase, respectively. The behaviour of the solid matrix is assumed to be governed by the generalized effective stress tensor σ' through combinations of mechanical stresses and fluid pressures [23, 24]:

$$\sigma' = \boldsymbol{\sigma} - p_g\mathbf{I} + S_r(p_g - p_w)\mathbf{I} \tag{21}$$

The term $(\boldsymbol{\sigma} - p_g\mathbf{I})$ is called the net stress, whereas $(p_g - p_w)$ is the matrix suction.

In this Lagrangian approach, the Cauchy strain tensor is used:

$$\boldsymbol{\varepsilon} = \frac{1}{2}\left(\mathbf{L} - \mathbf{L^T}\right) \tag{22}$$

where $\mathbf{L} = \frac{\partial \mathbf{u}}{\partial \mathbf{X}}$ is the displacement ($\mathbf{u}$) gradient defined in the global axis ($\mathbf{X}$) in the current moving configuration [14]. This strain tensor is related to the generalised effective stress tensor through the mechanical constitutive model:

$$d\sigma' = \mathbf{C} : d\varepsilon \tag{23}$$

where $\mathbf{C}$ is the mechanical constitutive tensor. This last equation is written in incremental form due to the non-linear behaviour of the solid matrix.

2.3. Mechanical constitutive model

The mechanical model, called ACMEG-TS [13], is based on an elasto-plastic framework, the total strain increment $d\varepsilon$ being decomposed into non-linear, thermo-elastic, $d\varepsilon^{e}$ and plastic, $d\varepsilon^{p}$, components. The elastic part of the deformation is expressed as follows:

$$d\varepsilon^{e} = \mathbf{E}^{-1}d\sigma' - \boldsymbol{\beta_T}dT \tag{24}$$

The first term of Equation (24) is the contribution of the effective stress increment $d\sigma'$ to the total elastic strain increment, through the non-linear elastic tensor $\mathbf{E}$. This tensor is based on two hypo-elastic moduli which depend on the effective pressure, the bulk modulus K, and the shear modulus G.

$$K = K_{ref}\left(\frac{p'}{p'_{ref}}\right)^{n^{e}} \quad \text{and} \quad G = G_{ref}\left(\frac{p'}{p'_{ref}}\right)^{n^{e}} \tag{25}$$

where K_{ref} (resp. G_{ref}) is the bulk modulus (resp. the shear modulus) at the reference mean effective stress p_{ref}, and n^{e} is the elastic exponent which governs the influence of mean effective stress on elastic stiffness.

According to Equation (21), this part may follow from total stress or fluid pressure variations. The second term of Equation (24) is related to the thermo-elastic strain of the material, through the thermal expansion coefficient matrix, $\boldsymbol{\beta_T} = (1/3)\beta'_{s}\,\mathbf{I}$, with β'_{s} as the volumetric thermal expansion coefficient.

The plastic strains in the material are induced by two coupled hardening processes: an isotropic and a deviatoric one. Using the concept of multi-mechanism plasticity, both mechanisms may induce volumetric plastic strain [25]. Therefore, the total volumetric plastic strain rate $d\varepsilon_{v}^{p}$ is the coupling variable linking the two hardening processes. The yield functions of the two mechanical plastic mechanisms have the following expressions (see Figure 2):

$$f_{iso} = p' - p'_{c}\,r_{iso} \quad ; \quad f_{dev} = q - Mp'\left(1 - b\,\text{Log}\,\frac{d\,p'}{p'_{c}}\right)r_{dev} = 0 \tag{26}$$

where p' is the mean effective stress, q is the deviatoric stress, and p'_{c} is the preconsolidation pressure. b, d, and M are material parameters. p'_{c} depends on temperature T and suction s in addition to the volumetric plastic strain, ε_{v}^{p}, that introduces thermoplasticity and suction-induced plasticity [26]:

$$p'_{c} = \begin{cases} p'_{c0}\exp\left(\beta\,\varepsilon_{v}^{p}\right)\{1 - \gamma_T\log[T/T_0]\} & \text{if } s \leqslant s_e \\ p'_{c0}\exp\left(\beta\,\varepsilon_{v}^{p}\right)\{1 - \gamma_T\log[T/T_0]\}\{1 + \gamma_s\log[s/s_e]\} & \text{if } s \geqslant s_e \end{cases} \tag{27}$$

where p'_{c0} is the initial preconsolidation pressure at ambient temperature T_0 and for suction lower than the air-entry value s_e. β is the plastic compressibility modulus, defined as $\beta = \beta_m + \Omega. s$ (β_m being the plastic compressibility upon saturated condition) and γ_T and γ_s are material parameters.

r_{iso} and r_{dev} are the degree of mobilization of the isotropic and the deviatoric mechanisms and are hyperbolic functions of the plastic strain induced by the isotropic and the deviatoric mechanisms, respectively [25, 27]. This enables a progressive evolution of the yield limit during loading and a partial release of this limit during unloading.

The flow rule of the isotropic mechanism is associated, whereas the deviatoric one is not and assumes the following forms:
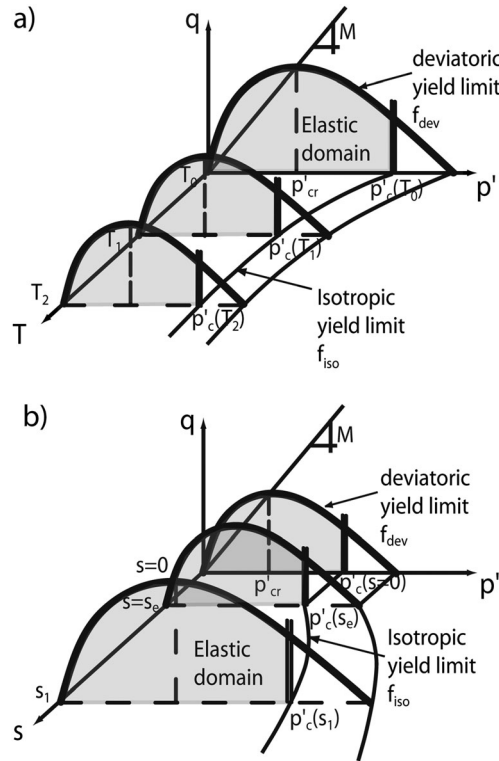
Figure 2. Effect of (a) temperature and (b) suction on the shape of coupled mechanical yield limits.

$$d\boldsymbol{\varepsilon}^{\mathbf{p,iso}} = \frac{\lambda^p_{iso}}{3}\mathbf{I} \tag{28}$$

$$d\boldsymbol{\varepsilon}^{\mathbf{p,dev}} = \lambda^p_{dev}\frac{1}{Mp'}\left[\frac{\partial q}{\partial \sigma'} + \alpha\left(M - \frac{q}{p'}\right)\frac{1}{3}\mathbf{I}\right] \tag{29}$$

The plastic multipliers, λ^p_{iso} and λ^p_{dev}, are determined using Prager's consistency equation for multi-dissipative plasticity [28, 29]. α is a material parameter.

2.4. Water retention constitutive model

In terms of water retention response, desaturation is also a yielding phenomenon. Hysteresis in water retention behaviour is modelled as a plastic process. As long as the soil is drying, suction increases, and the degree of saturation, S_r, tends to decrease mainly when the air-entry suction s_e is reached. Under re-wetting, a hysteretic phenomenon occurs, also represented by a yielding process (Figure 3). A wetting–drying cycle activates two successive yield limits in the $(S_r - s)$ plane (f_{dry} and f_{wet}, along the drying and wetting paths, respectively):

$$f_{dry} = s - s_d = 0 \quad ; \quad f_{wet} = s_d s_{hys} - s = 0 \tag{30}$$

where s_d is the drying yield limit and s_{hys} is a material parameter considering the size of the water retention hysteresis. Because air-entry suction of the materials depends on temperature and dry density, s_d is a function of temperature T and volumetric strain ε_v [13]:

$$s_d = s_{d0}\{1 - \theta_T \log[T/T_0] - \theta_e \log[1 - \varepsilon_v]\} \tag{31}$$

where θ_T and θ_e are material parameters describing the evolution of air-entry suction with respect to temperature and volumetric strain, respectively. If the initial state is saturated, the initial drying limit s_{d0} is equal to air-entry suction s_e and increases when suction overtakes s_e as follows:
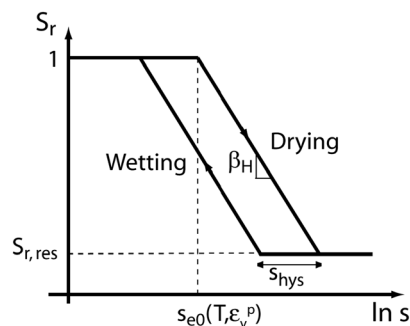
Figure 3. Schematic representation of water retention curve modelling.

$$s_{d0} = s_e \exp(-\beta_h \, \Delta S_r) \tag{32}$$

where β_h is the slope of the desaturation curve in the $(S_r - ln \, s)$plane (see Figure 3). The evolution of s_d with respect to T and ε_v is described by Equation (31).

3. MATERIAL CHARACTERISTICS

3.1. FEBEX bentonite

The clay barrier was constructed with highly compacted FEBEX bentonite blocks with an initial void ratio of 0.6 and an initial water content between 12.5% and 15.5%, corresponding to an initial suction of 110 to 130 MPa [4]. This corresponds to an initial dry density of the blocks of around 1700 kg m^{-3} and a degree of saturation between 35% and 45%. The THM properties of the FEBEX bentonite have been extensively investigated over the last decade. Its mechanical behaviour under non-isothermal and unsaturated conditions has been characterised by means of several experimental programs by Villar, Lloret, Romero and co-authors [4, 30–36].

The results of these studies have shown that, on the mechanical side of the problem, the simulation of the confined swelling behaviour of bentonite is the most important feature to reproduce. Pintado [37] performed swelling pressure tests in oedometric conditions on samples of FEBEX bentonite that were less compacted than were the blocks used in the *in situ* experiment. Depending upon density and suction, swelling pressures of blocks ranged from 3 to 10 MPa. Lloret *et al.* [4] compiled various tests on the same bentonite that show a strong dependency of swelling pressure on dry density. The experiments reported in Ref. [4] allowed not only to get final swelling pressures but also to follow the evolution of stresses induced by decreasing suction. Three successive trends were identified by Lloret *et al.* [4], but they are not yet fully physically explained (plastic strains, microstructural evolution of the material, etc.). However, comparison between simulation and experimental results, shown in Figure 4, reveals that the ACMEG-TS model provides an efficient framework for the understanding of the processes. The first and third zones can be well reproduced by a non-linear elastic behaviour, whereas the slight decrease of swelling pressure in the second zone may be interpreted by plastic strain generation (wetting collapse). The drastic increase of stress in the first zone is characteristic of constrained swelling of a rigid material (high bulk modulus under high suction) that turns into high stresses. In the third zone, the intensity of the stress increase is smaller because the rigidity of the bentonite is lower (low bulk modulus under low suction). In the second zone, plastic phenomena produce softening of the bentonite that induces a decrease of the swelling pressure. However, in this second zone, the ACMEG-TS model produces brutal change of behaviour that does not perfectly reflect the experimental trends. On the whole wetting path, the model nevertheless allows representing three key aspects: the initial rapid increase in pressure, its final value, and the distinction into three characteristic zones. Due to the difference in initial dry density between the laboratory experiment and the emplaced bentonite blocks, it has been decided to
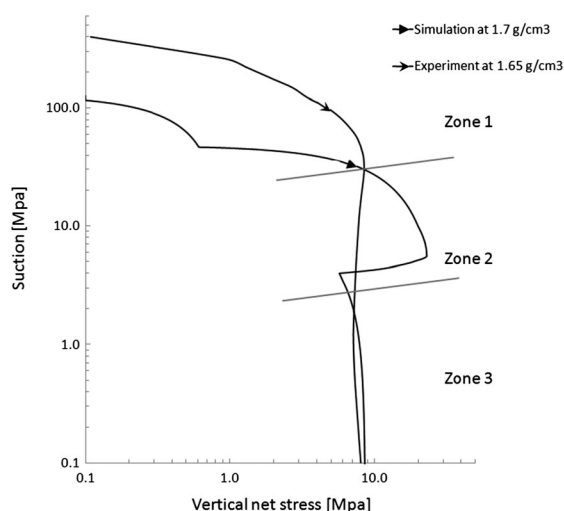
Figure 4. Behaviour of the simulated bentonite during a constrained swelling test and comparison with a similar experiment.

calibrate the model with a 9-MPa swelling pressure, which corresponds to the initial dry density of the blocks, that is, $1700\,\mathrm{kg\,m^{-3}}$, according to the trend reported in Ref. [4].

Another important feature in the simulated scenario is the thermal response of the materials. Ref. [32] provides the necessary information concerning the thermal expansion of compacted FEBEX bentonite. A conservative value has been chosen according to this document of $2.1 \times 10^{-4}\,\mathrm{K^{-1}}$ (volumetric coefficient) to mitigate the absence of gaps in the simulation, whereas some construction gaps exist in the actual experiment. Even if this value of elastic thermal expansion fits well with experimental observations, the value is very high compared with that of other kinds of soil. It is probably related to the thermal expansion of adsorbed water that can be assumed as a part of the solid skeleton. Consequently, upon heating, the constrained thermal dilatation of the bentonite in the confined gallery will produce high stress, partially compensated by thermoplasticity.

The simulation of thermal response oedometric tests is performed and compared with various experiments in Figure 5.

A series of numerical simulations of oedometric tests on hydraulic and mechanical paths have been performed to evaluate the behaviour of the simulated bentonite in usual cases that are different from the situation encountered by the material in the experiment. Numerical simulations of oedometric compression tests at different suction levels and ambient temperatures are shown in Figure 6. The initial strain observed at a net stress of 0.1 MPa is due to the suction changing from 127 MPa to the
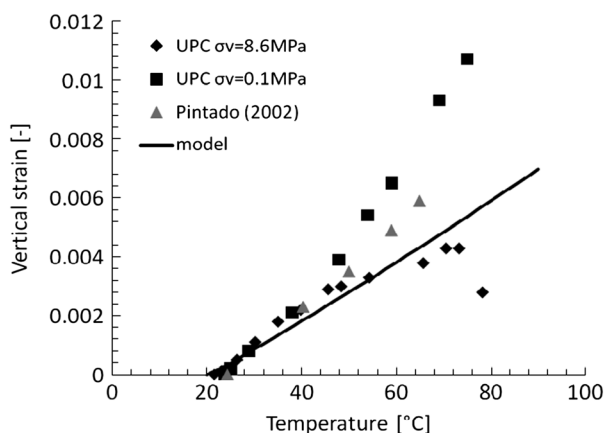

Figure 5. Thermally induced vertical strains in oedometric conditions. Experiments taken from Romero *et al*. [36] and Pintado *et al*. [37].
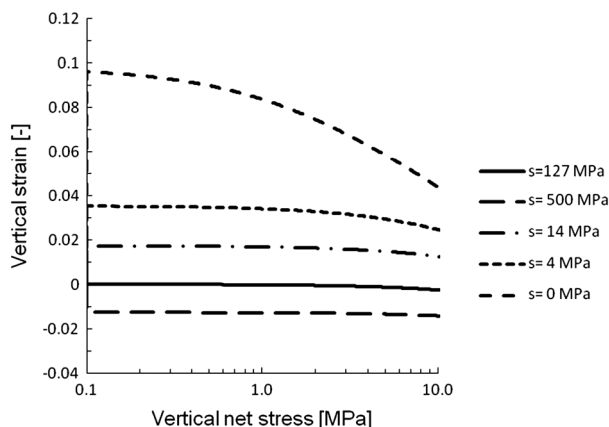
Figure 6. Numerical simulation of oedometric compressions on FEBEX bentonite at different suctions.

suction applied during compression. The subsequent compression paths clearly show the enhancement of the elastic domain with increased suction. Figure 7 reproduces the water retention curve observed on wetting at three different constant temperatures and compares the results with numerical simulations. In the S_r–s plane, the shift of the wetting curve to the left with increased temperature is well reproduced by the model. Figure 8 illustrates water retention hysteresis in addition to the effect of density. At a given suction, the wetting path occurs at a lower degree of saturation than do the drying paths, which is representative of the hysteretic response of soil in the S_r–s plane. For the simulation of tests on bentonite at a dry density of 1.7 kg/m^3, a preliminary volumetric plastic strain of 3%, corresponding to an increase in dry density from 1.65 to 1.7 kg/m^3, induces a shift to the right of the subsequent wetting line; hence, the denser the soil, the higher the degree of saturation for the same suction.

This range of experiments and choices enabled calibration of the model with parameters defining the mechanical and water retention behaviour, as presented in Table I. It should be noted that due to the lack of information on the shear behaviour of the material, the deviatoric mechanical parameters have been assigned with usual values for such a kind of clay.

The parameters governing the thermal and hydraulic diffusion in FEBEX bentonite are established from a review of the literature. Villar [31] reported the saturated hydraulic conductivity as a function of dry density. Good agreement between the Kozeny–Carman relationship (Equation (14)) and the
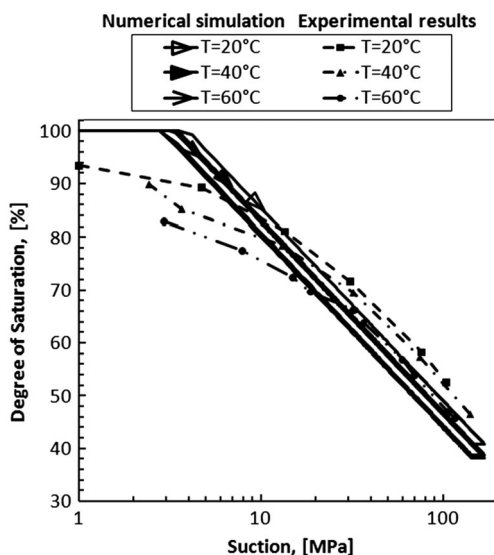

Figure 7. Numerical simulations of retention curves of FEBEX bentonite at different temperatures and comparison with experiments. Experimental curves from Lloret *et al.* [4].
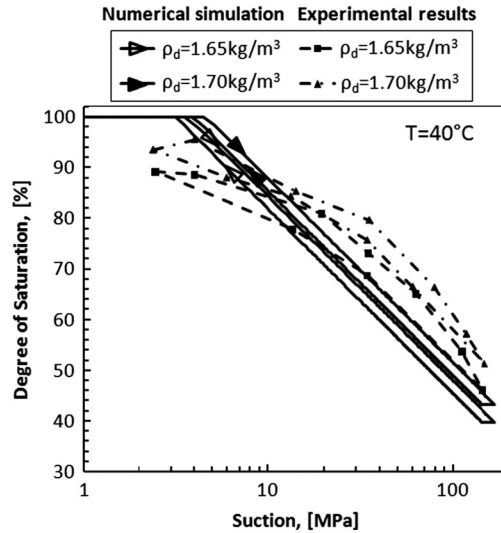
Figure 8. Numerical simulation of retention curves of FEBEX bentonite at two different dry densities and comparison with experiments. Experimental curves from Lloret *et al.* [4].

Table I. Set of FEBEX bentonite parameters for ACMEG-TS model.

Elastic parameters		
K_{ref}, G_{ref}, n^e, β'_s	[MPa], [MPa], [–], [°C^{-1}]	40, 18.5, 1, 2.1×10^{-4}
Isotropic plastic parameters		
β_m, γ_s, γ_T, r^e_{iso}, p'_c, Ω	[–], [–], [–], [–], [MPa] , [–]	10, 10, 0.2, 0.7, 2.2, 10^{-6}
Deviatoric plastic parameters		
$b,d,M,g,\alpha,a,r^e_{dev}$	[–], [–], [–], [–], [–], [–], [–]	1, 1.5, 1.2, 0, 1, 0.001, 0.8
Water retention parameters		
$s_{e0},\beta_h,\theta_T,\theta_e,s_{hys}$	[MPa], [–], [–], [–], [–]	4, 6.33, 0.1, 5, 0.9

evolution of permeability with dry density can be obtained for $k_{w0,sat} = 4 \ 10^{-14}$m/s, which corresponds to $n_0 = 0.37$ (i.e., $\rho_d = 1.7$ g/cm^3) and EXPN=EXPM=6.5 (Figure 9).

In addition, the water permeability depends upon the degree of saturation of the bentonite. Through a back-analysis of thermo-hydraulic bentonite properties, Pintado *et al.* [37] determined that Equation (14) provided the best agreement with CKW1=2.9.

The thermal diffusion of each phase has been calibrated to reproduce the experimental evolution of the thermal diffusion of the bentonite with respect to its degree of saturation (as reported in Ref. [5]), yielding the following parameters: $(\lambda_s \ ; \ \lambda_w \ ; \ \lambda_a) = (0.7 \ ; \ 2.1 \ ; \ 0) \ [W/(m°C)]$ (Figure 10). The heat capacity of the solid matrix is c_s=1091 J/(kg°C) [5].

Table II reports the material parameters of FEBEX bentonite in relation to the thermal and hydraulic diffusion processes. The parameters of the water retention curve have been previously defined in Table.

3.2. Granite

The Grimsel test site has been excavated in a predominately granite and granodiorite rock. Hydraulic and mechanical properties of the Aare massif granite have been compiled in several internal reports and have been partially reported by Alonso *et al.* (2005) [8] and Gens *et al.* [5] (see also [10, 38]). The mechanical behaviour of the granite is modelled by an elastic model. The water retention behaviour of granite is difficult to determine. Some laboratory test results show a low desaturation threshold (less than 1 MPa), whereas field measurements obtained during ventilation tests suggest that the air-entry value of the rock may in fact be much higher (up to 500 MPa) [5]. In our simulations, the granite is assumed to be fully saturated even under negative pore water pressure. So the option of a high air-entry value has been chosen. The mechanical, thermal, and hydraulic parameters of the granite are presented in Table II.
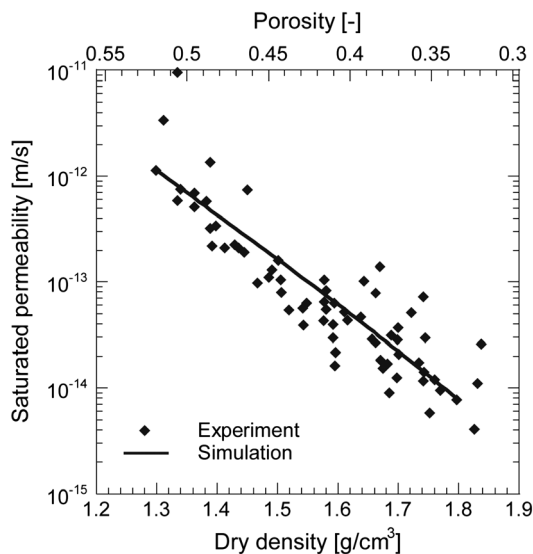
Figure 9. Effect of dry density on the saturated permeability of FEBEX bentonite considered with the Kozeny–Carman relationship. Comparison between the laboratory measurements [5] and simulation.
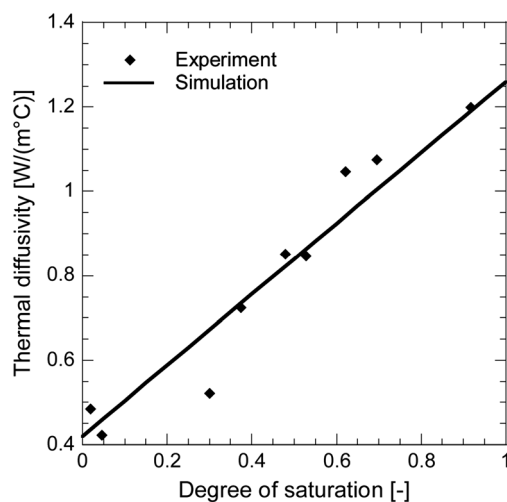

Figure 10. Effect of the degree of saturation on the thermal diffusivity of FEBEX bentonite. Comparison between the laboratory measurements [5] and simulation.

3.3. Other materials

The material parameters of the steel of the heaters, as well as the concrete of the plug, have been chosen in the range of usual parameters for those types of material. Their mechanical behaviour has been assumed to be linear elastic. The steel is considered as impervious and the concrete plug as fully saturated. Table II reports the chosen parameters for these two materials.

4. FEATURES OF THE ANALYSIS OF FEBEX *IN SITU* EXPERIMENT

The problem is treated under axisymmetric conditions around the y axis, which is the axis of the test drift (Figure 11), and consequently, gravity is not considered during computation. The distance of the external boundary to the engineered barrier is the same (60 m) in both the axial and radial

Table II. Parameters of the various materials involved in the simulation of the FEBEX *in situ* experiment.

Thermal parameters			Bentonite	Granite	Concrete	Canister
Solid thermal conductivity	λ_s	[W/(m °C)]	0.7	–	–	–
Water thermal conductivity	λ_w	[W/(m °C)]	2.1	–	–	–
Air thermal conductivity	λ_a	[W/(m °C)]	0	–	–	–
Global thermal conductivity	Γ	[W/(m °C)]	–	3.34	1.7	–
Solid heat capacity	$c_{p,s}$	[J/(kg °C)]	1091	–	–	–
Water heat capacity	$c_{p,w}$	[J/(kg °C)]	4200	–	–	–
Gas heat capacity	$c_{p,a}$	[J/(kg °C)]	1000	–	–	–
Global heat capacity	C_p	[J/(kg °C)]	–	1000	750	–
Liquid thermal expansion coefficient	β'_w	[°C^{-1}]	4×10^{-4}	4×10^{-4}	4×10^{-4}	–
Solid thermal expansion coefficient	β'_s	[°C^{-1}]	2.1×10^{-4}	2.5×10^{-5}	1×10^{-5}	2.5×10^{-5}
Hydraulic parameters						
Intrinsic water permeability	$k_{w0,sat}$	[m^2]	4×10^{-21}	4.5×10^{-19}	1×10^{-19}	
Kozeny–Carman coefficient 1	EXPM	[–]	6.5	0	0	–
Kozeny–Carman coefficient 2	EXPN	[–]	6.5	0	0	–
Relative permeability coefficient	CKW1	[–]	2.9	–	–	–
Volumetric parameters						
Initial porosity	n_0	[–]	0.4	0.01	0.15	0
Tortuosity	τ	[–]	0.5	0.6	0.6	
Solid specific mass	ρ_s	[kg/m^3]	2700	2660	2500	7800
Water specific mass	ρ_w	[kg/m^3]	1000	1000	1000	–
Air specific mass	ρ_a	[kg/m^3]	1.18	–	–	–
Liquid compressibility	$1/\chi_w$	[Pa^{-1}]	3.33×10^{-10}	3.33×10^{-10}	3.33×10^{-10}	–
Mechanical parameters						
Young elastic modulus	E	[MPa]	See Table	5000	3000	20000
Poisson ratio	υ	[–]		0.35	0.2	0.3

directions. The modelled domain is sufficiently large to avoid the undesired effects of the imposed boundary conditions in the far field and to model the dissipation of pore water pressure during the excavation stage. The first stage of the simulation is a preliminary hydromechanical calculation of the excavation phase. The goal is to obtain the initial pore water pressure in the host granite, during the ventilation of the drift, and also to get realistic stresses in the host rock, while keeping the radial stress along the drift at zero. An initial isotropic total stress of 28 MPa is imposed on the granite, as measured *in situ* at the depth of the drift. The water pressure is initially equal to 0.7 MPa over the whole domain and is brought to the atmospheric pressure on the drift surface for 1000 days. Local variations of stresses and pressures due to gravity in the modelled domain are neglected. The anisotropic stress state has not been considered in the simulation because of axisymmetric formalism. The initial temperature is equal to 12°C in the entire modelled domain.

Due to the phasing of construction, the bentonite, canisters, and plug elements are not included in the mesh during this first stage, as they are not present during the excavation and ventilation phase. The second stage begins with the introduction of these three elements.

The initial water pressure in the concrete plug is assumed to be at atmospheric pressure. In the bentonite, suction of 114 MPa is considered as the initial hydraulic condition. The external total stress is initially equal to zero at the beginning of the second stage. This corresponds to a generalised mean effective stress of 53.9 MPa, equal to the product $S_r \times s$ at the initial temperature (Equation (21)). The bentonite is assumed to be normally consolidated ($p'_{c0} = 2.2$ MPa; $\gamma_s = 10$; $s_0 = 114$ MPa). The canister and the concrete plug are also under zero stress. The air pressure has been fixed to atmospheric pressure over the entire unsaturated domain, as the experiment was not gas tight and possible corrosion gases are neglected during this experiment.

In the computation, the construction gap, evaluated as 5.53% of the emplacement volume [8], has not been considered. This implies that the swelling pressure predicted by the numerical simulations will be overestimated. This swelling caused by progressive wetting starts with this second stage and lasts 4 months before heating begins.

In the experiment, the temperature ramp was imposed with a controlled power (1200 W per heater for 20 days and 2000 W per heater over the following 33 days until reaching the desired temperature
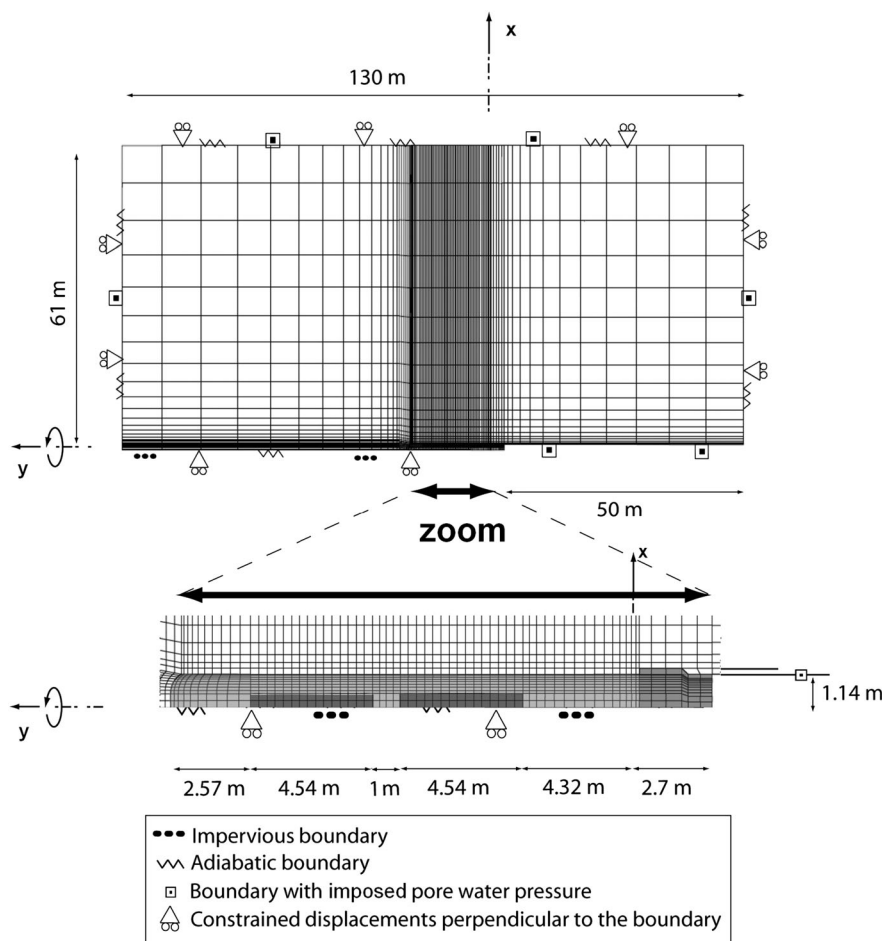
Figure 11. Finite element mesh used in the simulation of the *in situ* FEBEX experiment. The *y* axis is the axis of symmetry of revolution (*y* = 0 corresponds to the bentonite/plug contact).

of 100°C). The same scheme has been reproduced in the simulation. The thermal losses due to the presence of air in the construction gaps (which are located mainly inside the tube containing the heaters and at the frontier between bentonite and granite) could be estimated at 15%. Therefore, the power applied in the simulation is only 85% of the real power, with the same ramp up, and the centre of the heaters reaches 100°C at the correct time. The temperature on all heater nodes is then kept constant for the rest of the simulation, which allows maintaining the small variations in heater temperature between the corners and centre. The simulation has been performed on the total time of operation (i.e., 5 years). For all subsequent graphs, zero time corresponds to the start of the heating (27 February 1997).

5. RESULTS OF SIMULATION COMPARED WITH MEASUREMENTS

Figure 12–15 compare numerical results to experimental measurements at various locations. The indicated letters in the figures correspond to sections and are shown in Figure 1. The associated number corresponds to the radial rank of the node: 0 is for the centre of the tunnel, 2 is for the heater radius, 10 is for the frontier between the bentonite and granite, and higher numbers are located in the granite. The nodes are chosen for their proximity to the actual sensors.

Figure 12 presents the evolution of temperature over time in three sections of the engineered barrier and in one borehole in the rock mass. The temperatures at points F2-2 and I-2, being on the heater surface, remain constant in the last phase, but with a clear difference. The decrease of experimental temperature at point I-2 is mainly due to the power regulation being based on a different point and
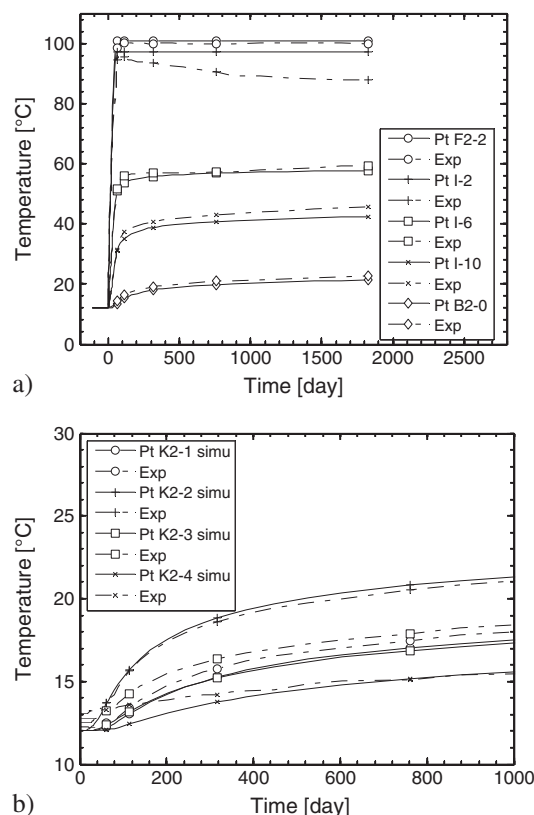
Figure 12. Variation of temperature with time at five points (distributed in three sections) of the engineered barrier and in one borehole in the host rock. Comparison between numerical simulation (full lines) and experimental measurements (dashed lines).

is not reproduced here. In section I, we observe a steady thermal gradient of about $50\,^\circ$C across 66 cm after 500 days (from $95\,^\circ$C at $x = 0.48$ m to $45\,^\circ$C at $x = 1.14$ m). On the other hand, far away from the heater (section B2, Figure 12a, and boreholes K1 and K2, Figure 12b), the temperature continuously increases, even after 5 years of heating. The results of the simulation show good agreement with *in situ* measurements.

The relative humidity in the bentonite is obtained in the simulation from the temperature and suction through Kelvin's law. Figure 13 displays the comparison between the measured and the computed values in two different sections of the engineered barrier. The simulated processes are also presented before zero time: the resaturation of bentonite before the defined zero time explains why both the experimental and simulated fields are not uniform at the start of heating. The simulation starts from a homogeneous relative humidity field of about 40% (corresponding to $s = 114$ MPa and $T = 12\,^\circ$C), and in the simulation, wetting starts immediately at the frontier between the granite and bentonite because of the water flow from the saturated granite to the unsaturated bentonite. It can be seen from the comparison between points F2-9 (Figure 13a), H-9 (Figure 13b), and C-9 (Figure 13c) that the experimental evolution of relative humidity largely depends on the presence of a construction gap close to the sensor (as at point F2-9) or lack thereof (see point C-9, which is already almost saturated at zero time). The sensor measurements show an initial gradient of relative humidity in each section, which is closely matched by the simulations. Close to the heater, the bentonite is dried due to thermally induced water evaporation (Figure 13a). Vapour arising from that drying diffuses outward and condensates in the cooler region, causing accelerated wetting of the bentonite in the central part. In addition, the more heated bentonite initially dilates and pressurises the more central one, therefore increasing the relative humidity at the centre. This effect is clearly shown in the wetting rate at points F2-6 (Figure 13a) and H-6 (Figure 13b), before and after the heating. A rapid increase from 40% to 60% is observed, whereas the trend before heating indicated a very slow
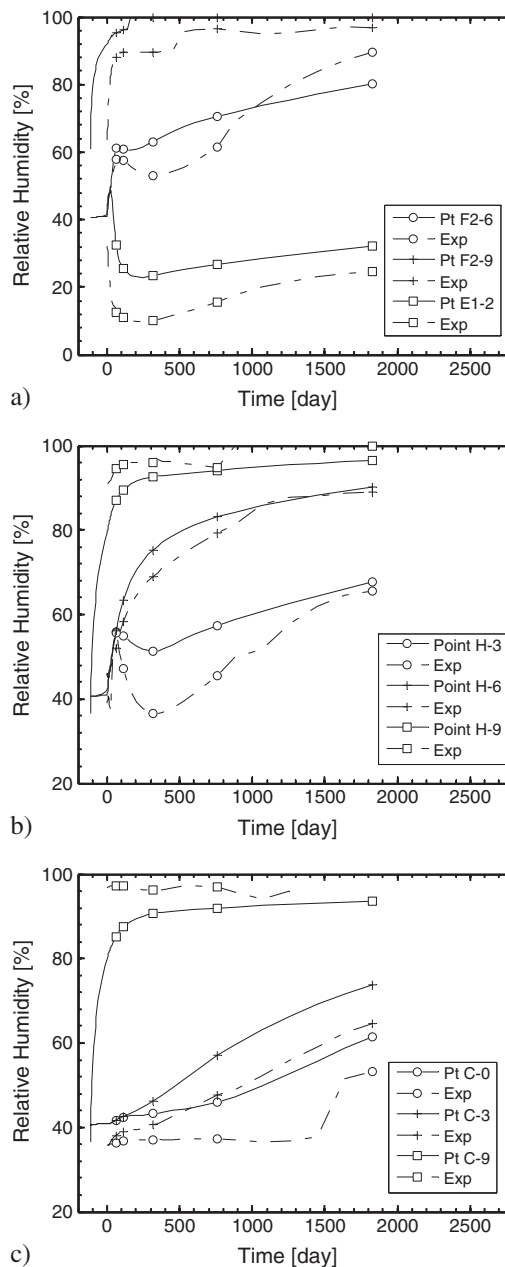
Figure 13. Variation of relative humidity with time at nine points distributed between heater and host rock (a), in the section between heaters (b), and in a section far from the heaters (c). Comparison between numerical predictions (full lines) and experimental measurements (dashed lines).

increase. Close to the granite, the effect of temperature on the resaturation of bentonite is not so obvious, as its evolution does not seem to be affected by heating at time t_0.

Figure 14 displays the evolution of principal stresses at a point in a borehole in section G, at a radial distance around 3 m, and resets to zero at zero time. As this local measurement is relatively far from the swelling buffer, we observe a continuous increase of radial stress and a simultaneous initial decrease of circumferential stress, as expected in a bored tunnel due to stress redistribution. The evolution of axial stresses is slightly slower, and its value is between that of radial and circumferential stresses, which is the correct behaviour in such a case. The simulation shows relatively good agreement with the sensors, given the uncertainties on this kind of measurements and the mechanical assumptions made in the simulation (no construction gap allowing some free swelling of the bentonite). The most important
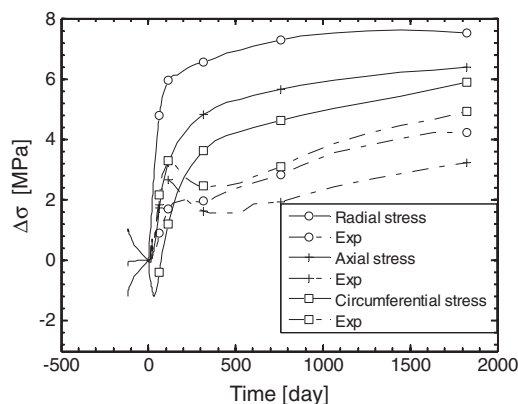
Figure 14. Variation with time of stresses in a radial borehole in the middle section of the experiment at radial distances around 3 m. The reference state for all sensors is that of granite at heaters' start. Evolution between the excavation of the drift and this time is shown for reference. Comparison between numerical predictions (full lines) and experimental measurements (dashed lines).
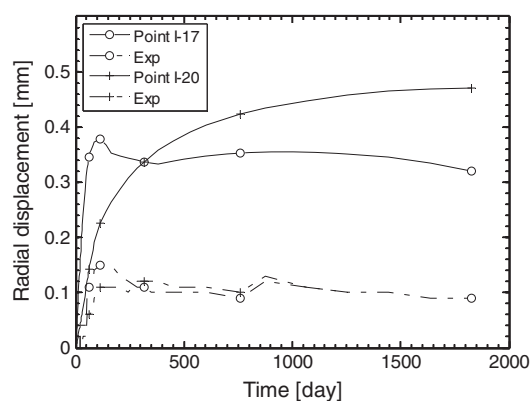

Figure 15. Variation with time of radial displacement (outwards positive) in a radial borehole in section I. Comparison between numerical predictions (full lines) and experimental measurements (dashed lines).

difference comes from the stress peak that is observed experimentally in these sensors. This peak can only be observed in the radial component of the stresses in the simulation, for points closer to the interface. This can be more clearly seen in Figure 15, which represents the radial displacements in a radial borehole, reset to zero at zero time. The peak in displacement induced by the peak in the swelling pressure of bentonite is clearly visible in both the simulation and experiment and was not observed in previous studies. Although its magnitude is greater than that of the experimental measurement, this is a very interesting feature of this model, which clearly reproduces the trend observed in reality.

6. INTERPRETATION OF THE NUMERICAL SIMULATIONS

The simultaneous heating (coming from the canister) and hydration (coming from the host formation) of the bentonite gives rise to interconnected phenomena that govern the complex response of the engineered barrier. The analysis of the numerical results permits a better understanding of these THM processes. In Figures 16–18, the evolution of the main THM variables is presented along the midplane section, perpendicular to a heater.

The thermal loading of the canister produces a rapid increase of temperature in the inner part of the engineered barrier, up to 100°C. At the outer part, the bentonite undergoes smaller temperature variations (up to 45°C) (Figure 16a). In that sense, the engineered barrier acts as a thermal buffer

aimed at reducing the temperature in the host formation. That positive effect of the bentonite avoids producing any significant thermally induced damage in the host formation. A quasi-steady-state thermal regime is rapidly reached in the bentonite. After less than 6 months, the temperature distribution tends toward equilibrium along the section considered.

At the inner boundary, the temperature increase produces, via water evaporation, a drying of the bentonite. Consequently, the degree of saturation decreases and suction increases. The suction rises up to more than 250 MPa after 6 months, as shown in Figure 16b. It corresponds to a drop in the degree of saturation down to 0.35 (Figure 16c). The decrease in the degree of saturation is relatively low due to two main effects: (i) The S_r–s relation is a logarithmic relation in the desaturation phase and, accordingly, a high increase of suction produces only a limited decrease of the degree of
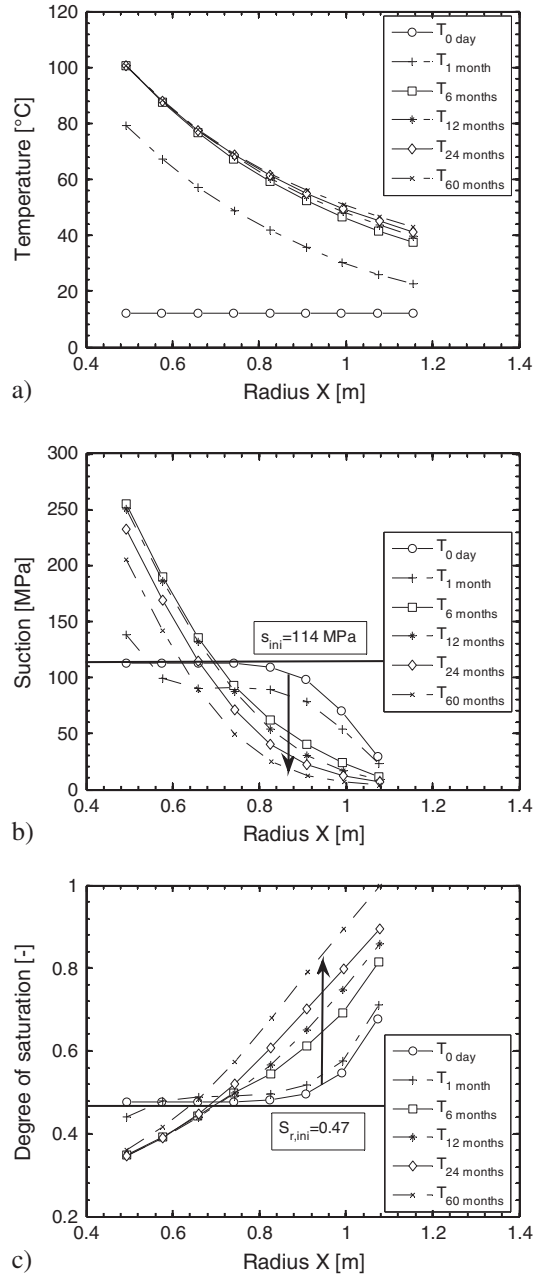

Figure 16. Evolution in bentonite of the computed temperature (a), suction (b), and degree of saturation (c) along the midplane section of a heater at six different moments.
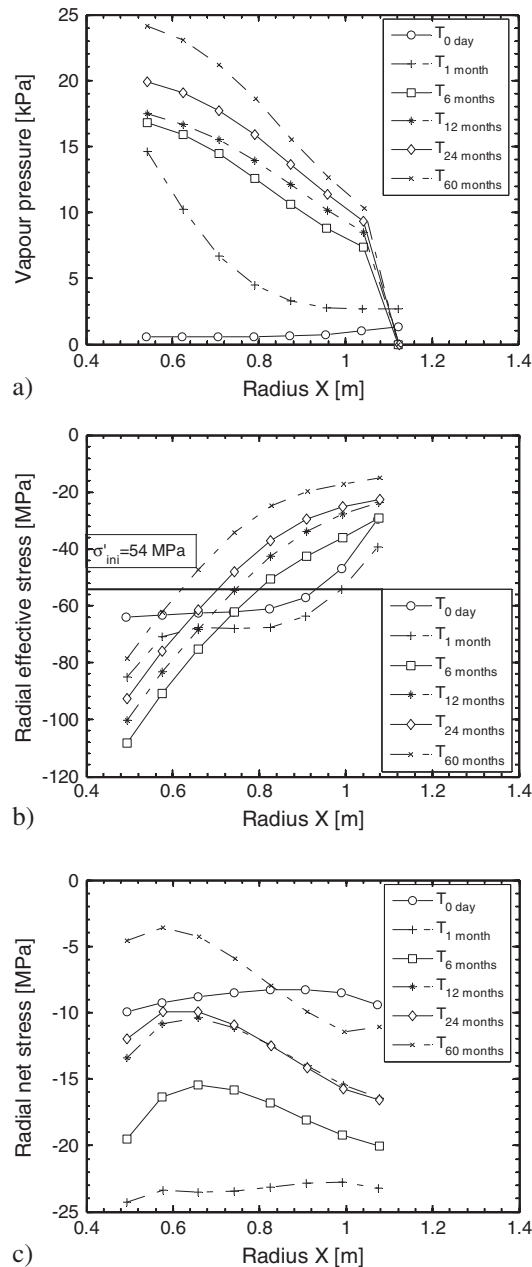
Figure 17. Evolution in bentonite of the computed vapour pressure (a), radial effective stress (b), and radial net stress (c) along the midplane section of a heater at six different moments.

saturation; (ii) through the effect of the volumetric strain on the water retention capacity, the bentonite drying produces shrinkage (i.e., decrease of the porosity) and a subsequent limitation of the decrease of the degree of saturation with suction.

At the outer boundary, the suction decreases and the degree of saturation increases. This is induced by two processes: (i) The higher water pressure of the granite than that in the buffer material implies a flow of water from granite to bentonite, this hydration process being the main contributor in the resaturation of the bentonite; (ii) in addition, the vapour arising from the drying of the inner region diffuses through the engineered barrier and condenses in the cooler zone. This explains the gradient of vapour pressures that can be seen in Figure 17a and the fact that it does not reach a steady state, as opposed to the steady state of temperature.
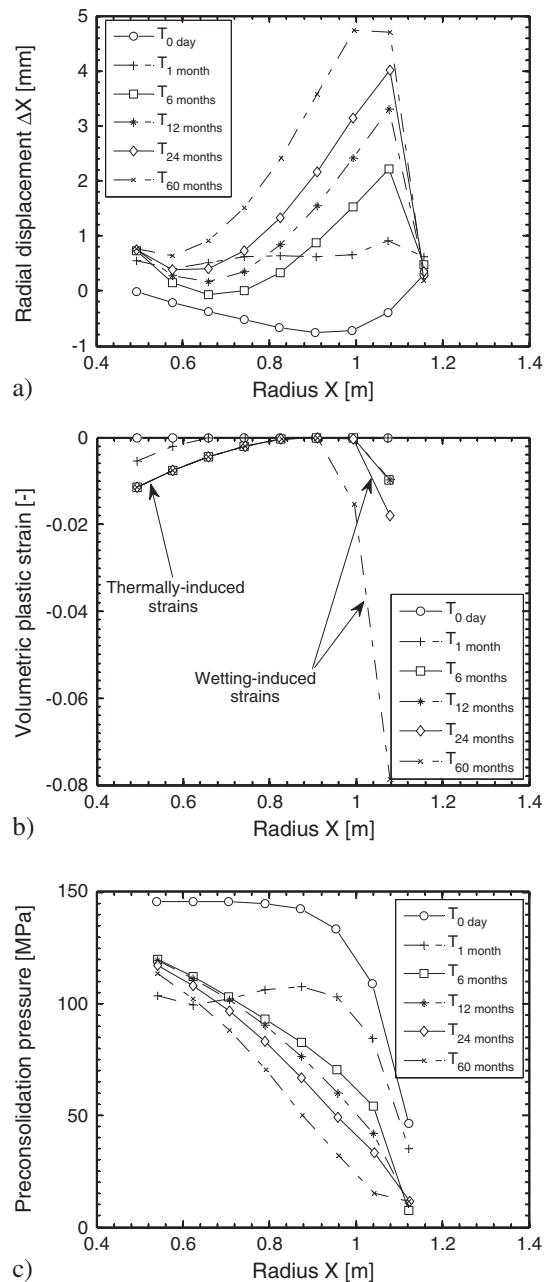
Figure 18. Evolution in bentonite of the radial displacement (a), volumetric plastic strains (b), and preconsolidation pressure (c) along the midplane section of a heater at six different moments.

An interesting transient effect occurs in the very short term. As thermal diffusion is faster than hydraulic diffusion in bentonite, the temperature produces an increase in the pore water pressure that has no time to dissipate in the short term. Consequently, after 1 month, the suction is lower than the initial suction almost everywhere in the domain (and the degree of saturation is higher) (Figure 16b and c). This transient effect dissipates by the means of hydraulic diffusion when the temperature reaches a quasi-steady-state regime.

The distribution of the radial effective stress (Figure 17b) is the sum of the radial net stress and the product $S_r \times s$ (Figure 16b and c). As a consequence, the drying process in the inner part induces an increase of the radial effective stress, whereas the hydration of the outer part decreases the radial

effective stress. In terms of the radial net stress (Figure 17c), the initial wetting immediately creates high stresses in the whole buffer (10 MPa after 4 months of isothermal wetting). The additional effect of temperature induces a maximum net stress at 1 month, before it decreases to reach a final level of around 8 MPa, consistent with the laboratory swelling pressure experiments.

In Figure 18a, the distribution of radial displacements shows a contraction of the bentonite in the inner part whereas the outer part dilates. The inner boundary value is imposed by the thermal dilatation of the heater and should be seen as a relative zero at each time to determine whether contraction or dilatation occurs in the buffer. The temperature-induced drying produces shrinkage whereas the hydration of the outer part produces swelling. In addition, the bentonite is also prone to plastic processes such as thermal and hydraulic collapse. The analysis of the volumetric plastic strains (as shown in Figure 18b) reveals that two phenomena are at play. On the inner side, these irreversible strains are produced by the drastic increase of the mean generalised effective stress in combination with the thermoplasticity. On the outer side, the plastic strains compensate the high elastic swelling pressure as discussed in Figure 4. In terms of radial displacement, the contraction of the inner part and the dilatation of the outer part produce a movement of the bentonite barrier (Figure 18a), and strong variations of density are observed between the inner half and the outer half.

Figure 18c exhibits the evolution of an internal material parameter of the ACMEG-TS model. The distribution of the preconsolidation pressure derives from the suction, the temperature, and the volumetric plastic strain generated (Equation (27)). Accordingly, the sudden decrease of suction during the first month of operation produces a drop in the preconsolidation pressure. Then, on both the outer and inner limits where plasticity occurs, the preconsolidation pressure is controlled by the consistency condition, imposing that under full activation of the isotropic plastic mechanism, the stress point lies on the isotropic yield limit. Thus, the preconsolidation pressure is equal to the mean generalised effective stress.

Figure 19 shows how the coupled phenomena influence the water retention behaviour of the bentonite in various locations. The effect of volume and temperature changes in the water retention capability could be explained as follows. The increase in temperature that is observed in the whole system leads to a slight decrease in water retention capability, as can be seen when the evolution at point F2-9 deviates from the linear trend (see highlight in the figure). A comparison between points that are subjected to a significant water flow (H-9 and F2-9) underlines volume change effects. At point F2-9, volume changes (wetting collapse) at the time of resaturation are limited and four times
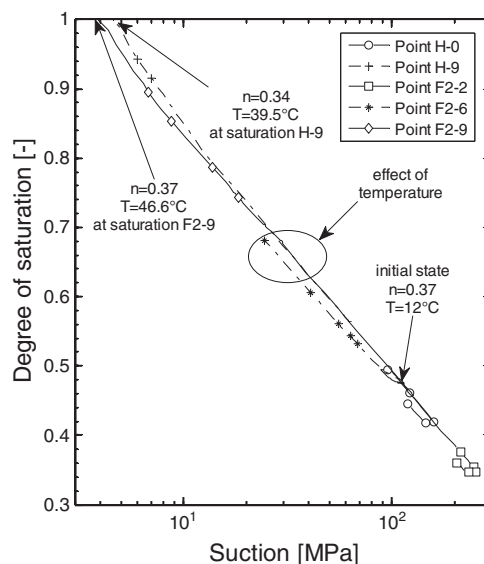

Figure 19. Water retention behaviour of bentonite during the experiment at five points distributed in two sections.

smaller than those at point H-9, and temperatures are similar. The resaturation curves are clearly different and underline the increased retention capability of the compacted material.

Point F2-2 is mainly under the influence of the heater, and water does not reach it before heating begins. It exhibits the typical water retention hysteresis and only one drying–wetting cycle. The points that are less strongly influenced by heat or water flow (F2-6 and H-0) undergo two cycles: they are first wetted and then dried by the effects linked to temperature as previously explained, and finally wetted again.

7. CONCLUSIONS

Facing the need to analyse and predict the long-term behaviour of underground disposal facilities for nuclear waste, the primary aim of this numerical analysis is to provide a means for assessing and understanding the thermal, hydraulic, and mechanical responses of bentonite and the surrounding rock involved in a multibarrier system. The interpretation of the THM processes requires comprehensive constitutive models and numerical tools to incorporate most of the material behavioural features.

The FEBEX *in situ* test is a near-to-real experiment of nuclear waste disposal in a granitic formation. The THM behaviour of the buffer material (made of FEBEX bentonite) and the surrounding host rock (granite), encountering many complex and interconnected THM phenomena, has been modelled by the means of finite element simulations.

The parameters of the thermoplastic constitutive model used for saturated and unsaturated conditions, named ACMEG-TS, have been retrieved from numerical simulations of a series of oedometric tests under controlled temperature and suction. Alternatively, the parameters for the thermal and hydraulic diffusion models were extracted from the literature.

The features of the numerical analysis have been presented. Subsequently, the obtained results have been compared with the available sensors measurements in both the engineered barrier and the granite. Despite the non-simulated construction gap, the results of the simulations show good agreement with the experiment. The confined swelling behaviour of highly compacted bentonite, including three distinct regimes, is well reproduced. It is an important feature of the ACMEG-TS model that results directly from the introduction of a wetting collapse mechanism in the framework of generalised effective stress.

In a second step, the results obtained were interpreted in the light of elasto-thermoplasticity of unsaturated materials. In particular, the effects of heating and wetting were highlighted, and the spatial and time distributions of their respective influence on the volumetric behaviour were shown. Moreover, the measurable consequences of the complexity of the water retention behaviour, which includes the effects of hysteresis, temperature, and mechanical strain, have been shown in terms of suction and mechanical effects.

These results highlight two major features of the behaviour of compacted bentonite that were considered here. The first aspect is the hysteretic water retention behaviour of bentonite, which, coupled with adequate modelling, allows for a proper reproduction of the evolution of relative humidity in the buffer. The second aspect is the complexity of the swelling behaviour of bentonite, which is tackled here with a new approach using the framework of suction-induced plasticity. This allows for a better understanding of experimentally observed behaviour while being a step toward more precise modelling. In such a way, the use of an advanced thermoplastic constitutive model using an unsaturated formalism significantly advances the knowledge of the highly coupled processes occurring in a clayey formation, initially unsaturated, in the near field of a heat-emitting radioactive waste.

REFERENCES

1. Laloui L, François B, Nuth M, Péron H, Koliji A. A thermo-hydro-mechanical stress-strain framework for modeling the performance of clay barriers in deep geological repositories for radioactive waste. Keynote paper. *1st European Conf. on Unsaturated Soils*, Durham, UK, 2008; 63–80.
2. Gens A, Vaunat J, Garitte B, Wileveau Y. In situ behaviour of a stiff layered clay subject to thermal loading: observations and interpretation. *Geotechnique* 2007; **57**(2):207–228.
3. François B, Laloui L, Laurent C. Thermo-hydro-mechanical simulation of ATLAS in situ large scale test in Boom Clay. *Computers and Geotechnics* 2009; **36**(4):626–640.
4. Lloret A, Romero E, Villar MV. FEBEX II Project: Final report on thermo-hydro-mechanical laboratory tests, Publicación técnica 10/2004, ENRESA, 165 p.
5. Gens A, Garcia-Molina AJ, Olivella S, Alonso EE, Huertas F. Analysis of a full scale in situ test simulating repository conditions. *International Journal for Numerical and Analytical Methods in Geomechanics* 1998; **22**(7):515–548.
6. Gens A, Guimarães LDN, Garcia-Molina A, Alonso EE. Factors controlling rock-clay buffer interaction in a radioactive waste repository. *Engineering Geology* 2002; **64**(2–3):297–308.
7. Gens A, Guimarães LDN, Olivella S, Sánchez M. Analysis of the THMC Behaviour of Compacted Swelling Clay for Radioactive Waste Isolation, In *Elsevier Geo-Engineering Book Series*, Stephansson O, Hudson J, Jing L (eds.), vol. **2**. Elsevier, London, UK, 2004; 317–322.
8. Alonso EE *et al*. The FEBEX benchmark test: case definition and comparison of modelling approaches. *International Journal of Rock Mechanics and Mining Sciences* 2005; **42**(5–6):611–638.
9. Sugita Y, Chijimatsu M, Ito A, Kurikaml H, Kobayashi A, Ohnishi Y. THM simulation of the full-scale in-situ engineered barrier system experiment in grimsel test site in switzerland. In *Elsevier Geo-Engineering Book Series*, Stephansson O, Hudson J, Jing L (eds.), vol. **2**. Elsevier, London, UK, 2004; 119–124.
10. Rutqvist J, Tsang CF. A fully coupled three-dimensional thm analysis of the febex in situ test with the rocmas code: prediction of thm behavior in a bentonite barrier. In *Elsevier Geo-Engineering Book Series*, Stephansson O, Hudson J, Jing L (eds.), vol. **2**. Elsevier, London, UK, 2004; 143–148.
11. Nguyen TS, Selvadurai APS, Armand G. Modelling the FEBEX THM experiment using a state surface approach. *International Journal of Rock Mechanics and Mining Sciences* 2005; **42**(5–6):639–651.
12. Gens A, Sánchez M, Guimarães LDN, Alonso EE, Lloret A, Olivella S, Villar MV. A full-scale in situ heating test for high-level nuclear waste disposal: observations, analysis and interpretation. *Geotechnique* 2009; **59**(4):377–399.
13. François B, Laloui L. ACMEG-TS: A constitutive model for unsaturated soils under non-isothermal conditions. *International Journal for Numerical and Analytical Methods in Geomechanics* 2008; **32**(16):1955–1988.
14. Charlier R, Radu J-P, Collin F. Numerical modelling of coupled transient phenomena. *Revue Française de Génie Civil* 2001; **5**(6):719–741.
15. Collin F, Li XL, Radu JP, Charlier R. Thermo-hydro-mechanical coupling in clay barriers. *Engineering Geology* 2002; **64**(2–3):179–193.
16. Panday S, Corapcioglu MY. Reservoir transport equations by compositional approach. *Transport in Porous Media* 1989; **4**(4):369–393.
17. Collin F. Couplages thermo-hydro-mécaniques dans les sols et les roches tendres partiellement saturés. *PhD Thesis*, Université de Liège in Department ArGEnCo, Liège, Belgium, 2003.
18. Collin F, Chambon R, Charlier R. A finite element method for poro mechanical modelling of geotechnical problems using local second gradient models. *International Journal for Numerical Methods in Engineering* 2006; **65**(11):1749–1772.
19. Charlier R. Approche unifiée de quelques problèmes non linéaires de mécanique des milieux continus par la méthode des éléments finis. *PhD Thesis*, Université de Liège in Department ArGEnCo, Liège, Belgium, 1987.
20. Gerard P, Charlier R, Chambon R, Collin F. Influence of evaporation and seepage on the convergence of a ventilated cavity. *Water Resources Research* 2008; **44**:W00C02.
21. Thomas HR, King SD. A non-linear, two-dimensional, potential-based analysis of coupled heat and mass transfer in a porous medium. *International Journal for Numerical Methods in Engineering* 1994; **37**(21):3707–3722.
22. Philip JR, De Vries DA. Moisture movement in porous materials under temperature gradients. *Transactions, American Geophysical Union* 1957; **38**:222–232.
23. Schrefler BA. The finite element method in soil consolidation (with applications to surface subsidence). *PhD Thesis*, University College, Swansea, UK, 1984.
24. Nuth M, Laloui L. Effective stress concept in unsaturated soils: Clarification and validation of a unified framework. *International Journal for Numerical and Analytical Methods in Geomechanics* 2008; **32**(7):771–801.
25. Hujeux J-C. Calcul numérique de problèmes de consolidation élastoplastique. *PhD Thesis*, Ecole Centrale, Paris, France, 1979.
26. Salager S, François B, El Youssoufi S, Laloui L, Saix C. Experimental investigations on temperature and suction effects on compressibility and pre-consolidation pressure of a sandy silt. *Soils and Foundations* 2008; **48**(4): 453–466.
27. Laloui L, Francois B. ACMEG-T: Soil Thermoplasticity Model. *Journal of Engineering Mechanics* 2009; **135**(9):932–944.
28. Prager W. Recent Developments in the Mathematical Theory of Plasticity. *Journal of Applied Physics* 1949; **20**(3):235–241.

29. Rizzi E, Maier G, Willam K. On failure indicators in multidissipative materials. *International Journal of Solids and Structures* 1996; **33**(20–22):3187–3214.
30. Villar MV. Investigation of the behaviour of bentonite by means of suction-controlled oedometer tests. *Engineering Geology* 1999; **54**(1–2):67–73.
31. Villar MV. Thermo-hydro-mechanical characterisation of a bentonite from Cabo de Gata: A study applied to the use of bentonite as sealing material in high level radioactive waste repositories, Publicación técnica 04/2002, ENRESA.
32. Enresa. Febex Project: Full-scale engineered barriers experiment for a deep geological repository for high level radioactive waste in crystalline host rock, Publicación técnica 1/2000, ENRESA, 354 p.
33. Lloret A, Villar MV, Sánchez M, Gens A, Pintado X, Alonso EE. Mechanical behaviour of heavily compacted bentonite under high suction changes. *Geotechnique* 2003; **53**(1):27–40.
34. Villar MV, Lloret A. Influence of temperature on the hydro-mechanical behaviour of a compacted bentonite. *Applied Clay Science* 2004; **26**(1–4):337–350.
35. Villar MV, García-Siñeriz JL, Bárcena I, Lloret A. State of the bentonite barrier after five years operation of an in situ test simulating a high level radioactive waste repository. *Engineering Geology* 2005; **80**(3–4):175–198.
36. Romero E, Villar MV, Lloret A. Thermo-hydro-mechanical behaviour of two heavily overconsolidated clays. *Engineering Geology* 2005; **81**(3):255–268.
37. Pintado X, Ledesma A, Lloret A. Backanalysis of thermohydraulic bentonite properties from laboratory tests. *Engineering Geology* 2002; **64**(2–3):91–115.
38. Sobolik S, Webb S, Kobayashi A, Chijimatsu M. Hydromechanical response of jointed host granitic rock during excavation of the febex tunnel. In *Elsevier Geo-Engineering Book Series*, Stephansson O, Hudson J, Jing L (eds.), vol. **2**. Elsevier, London, UK, 2004; 125–130.